

# Imaging surface contacts: power law contact distributions and contact stresses in quartz, calcite, glass and acrylic plastic

James H. Dieterich, Brian D. Kilgore

*U.S. Geological Survey, 345 Middlefield Road, Menlo Park, California, USA*

Received 8 March 1995; accepted 14 August 1995

---

## Abstract

A procedure has been developed to obtain microscope images of regions of contact between roughened surfaces of transparent materials, while the surfaces are subjected to static loads or undergoing frictional slip. Static loading experiments with quartz, calcite, soda-lime glass and acrylic plastic at normal stresses to 30 MPa yield power law distributions of contact areas from the smallest contacts that can be resolved ( $3.5 \mu\text{m}^2$ ) up to a limiting size that correlates with the grain size of the abrasive grit used to roughen the surfaces. In each material, increasing normal stress results in a roughly linear increase of the real area of contact. Mechanisms of contact area increase are by growth of existing contacts, coalescence of contacts and appearance of new contacts. Mean contact stresses are consistent with the indentation strength of each material. Contact size distributions are insensitive to normal stress indicating that the increase of contact area is approximately self-similar. The contact images and contact distributions are modeled using simulations of surfaces with random fractal topographies. The contact process for model fractal surfaces is represented by the simple expedient of removing material at regions where surface irregularities overlap. Synthetic contact images created by this approach reproduce observed characteristics of the contacts and demonstrate that the exponent in the power law distributions depends on the scaling exponent used to generate the surface topography.

---

## 1. Introduction

The processes that occur when rough surfaces are brought into contact are of fundamental interest for understanding a variety of rock properties. Contact processes control the friction and wear of surfaces and regulate the formulation of fault gouge. Elastic and anelastic deformation of contacts govern change of crack aperture which in turn affects the bulk properties of fractured or jointed rock masses including hydrologic properties of fractures, apparent elastic properties, electrical conductivity, seismic wave speed and seismic attenuation.

Characteristics of contacts between surfaces have been especially difficult to study experimentally. Generally the methods that have been employed to characterize surface contacts in rocks are based on post-experiment examination and involve some degree of invasion of the surfaces with inherent risk of altering the contacts. For example, Stesky and Hannan (1987) examined thin sections of epoxy-filled cracks that were subjected to large loads while the epoxy hardened. Logan and Teufel (1986) employed temperature-sensitive dyes to detect regions of contact that experienced local temperature rise during frictional slip. Nolte et al. (1989) injected molten

Woods metal into fractures while samples were under stress to make casts of the fractures which were later inspected. Finally, a number of studies (for example, Greenwood and Williamson, 1966; Walsh and Grosenbaugh, 1979; Brown and Scholz, 1985a; Carlson and Gangi, 1985) deduce contact characteristics through theoretical models which employ descriptions of surface topography (roughness).

This paper employs a method for imaging the actual areas of contact between roughened surfaces of transparent materials. Images are directly obtained during experiments on surfaces in static contact as well as surfaces undergoing frictional slip. A recent paper (Dieterich and Kilgore, 1994) presented initial findings on contact processes during frictional slip. In this study we describe a quantitative improvement to this method based on deconvolution of the digitized images and present data on contact size distributions and contact stresses. Materials investigated include quartz, calcite, soda-lime glass and acrylic plastic. We find power law distributions of contact sizes which carry implications for modeling of contacting surfaces and for scaling of laboratory results to geologic conditions.

**2. Experimental procedure**

The method for observing regions of contact between roughened surfaces of transparent materials is illustrated in Fig. 1. Contact is established only at isolated regions where the stresses are very high. Because the index of refraction of the samples is very different from the air gap between the surfaces, the roughened surfaces scatter transmitted light except where the surfaces are in contact. Hence, when viewed through a microscope the contacts appear as bright spots against a darker background. A similar technique for viewing surface contacts has been previously described (Kragelskii, 1965) but it appears to have been little used. With the emergence of digital imaging capabilities and computer aided image analysis, this method is well-suited for intensive quantitative investigation of contact processes.

We use the experimental apparatus and optical system described by Dieterich and Kilgore (1994). It consists of a modified double shear apparatus with cube-shape beam turners to provide an optical path

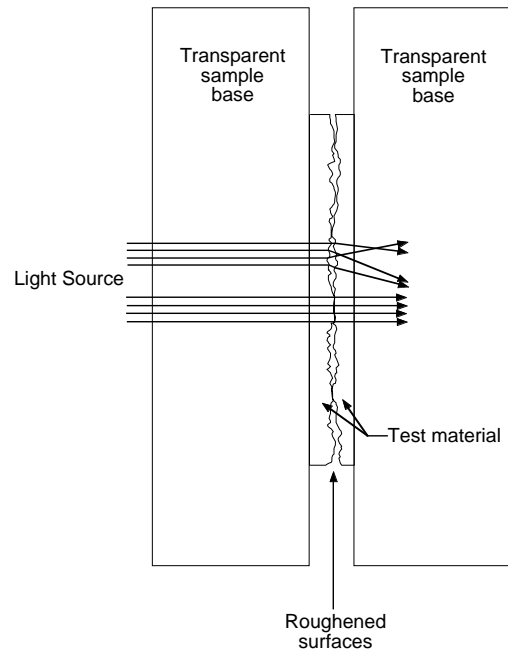


Fig. 1. Schematic representation of sample assembly with roughened contacting surfaces (not to scale). Light transmitted across the surfaces is scattered except at regions of contact.

through the samples and across the contacting surfaces. The beam turners support the normal stress applied to the samples (Fig. 2) permitting the surface to be viewed while subjected to normal stresses. The surfaces may be held in stationary contact or slipped

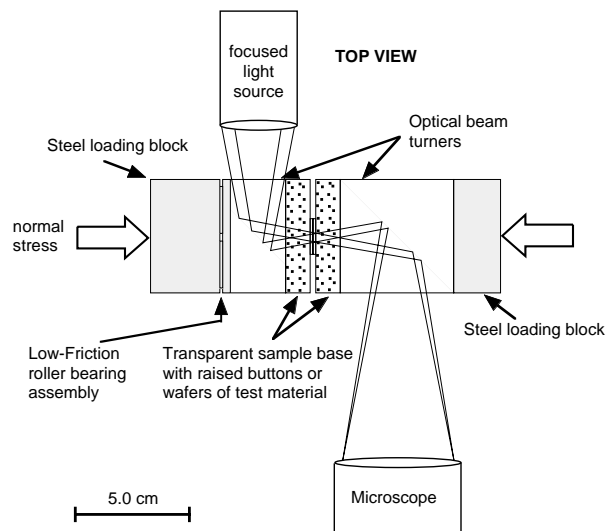


Fig. 2 Apparatus used in this study.

at servo-controlled sliding speeds from  $10^{-4}$   $\mu\text{m/s}$  to  $10^3$   $\mu\text{m/s}$ . This study concentrates on contact processes for stationary surfaces.

Tests with quartz and calcite employed thin optical grade wafers (15.8 mm x 15.8 mm x 1.5 mm) that were glued to a glass base 50 mm x 50 mm x 12 mm (Fig. 2) with a transparent epoxy adhesive formulated for strain gage applications. The quartz and calcite wafers were oriented with the optical *c*-axis perpendicular to the contacting surfaces (parallel to the observing direction) to minimize possible double refraction effects. The contacting surfaces of soda-lime glass and acrylic were on the face of a raised button (15.9 mm. X 15.9 mm) that was machined from single blocks of these materials. With each material, the contacting surfaces were roughened by hand lapping with #60, #100 or #240 silicon carbide abrasive and water to produce surfaces of varying roughness. Henceforth, the surfaces will be designated simply as #60, #100 or #240 surfaces to indicate the abrasive used in lapping.

In the following we refer to the nominal average normal stress applied to the surfaces simply as normal stress *s*. The average normal stresses supported by the regions of actual contact between the surfaces is referred to as the contact stress *s<sub>c</sub>*. Normal stresses to 30 MPa were employed for this study.

The observation system employs a long working distance microscope fitted with a still camera, a high resolution monochrome video camera (640 X 480 pixels), and a photovoltaic silicon photodiode. See Dieterich and Kilgore (1994) for use of the photodiode to obtain continuous measures of contact area during an experiment. The video images were captured in digital form (256 gray levels) for subsequent computer processing. The illuminating light source utilizes a focusing system matched to the microscope optics to minimize point diffraction effects. Most experiments use a narrow bandwidth (10 nm) interference filter (550 nm center wavelength) which slightly improved image quality through removal of chromatic aberration. Except for calcite, which yielded somewhat poorer image quality than the other materials, minimum resolved contact size is one pixel which corresponds to a surface region of  $1.88 \times 1.88 \mu\text{m}$ .

Measurements of contact numbers, contact area distributions, net area of contact and mean contact

stress are obtained from the digitized video images of the surfaces. The analysis procedure is based on converting the gray-level digitized images to only black or white to separate areas of low light transmission (no contact) from areas of high light transmission (contacts). This procedure requires determination of an appropriate threshold light intensity at the contact boundaries to define the contact areas. Threshold intensity is ascertained by comparing the digitized video images with direct through-the-microscope visual observations of the contacts. Automated analysis of the black and white contact images of contacts was then performed on a Macintosh IIfx computer using *Image*, a public domain computer program developed by W. Rasband at the National Institutes of Health.

While analysis of the video images is straight-forward in principle, several complications may arise in practice. Among these are human variability in setting the threshold intensity used to define the regions of contact, non-uniform illumination across the field of observation, various optical scattering and resolution effects and sampling error which results from imaging only a portion of the surface together with non-uniform spatial distribution of contacts. Optical effects and setting of the threshold light intensity are taken up in the following section of this report. Care was exercised in design of the illumination system and errors in determination of net contact area due to non-uniform illumination are approximately  $\pm 0.05$  or less of the total inferred contact area, which is small compared to the other sources of error.

Because the images sample only a portion of the sliding surface, an important source of uncertainty and scatter in measurement of contact area arises from variation of the density of contacts by location on the surface. Non-uniform contact density appears to be caused by non-uniform distribution of the normal stresses between the surfaces arising from sample misalignment and from long wavelength topographic features that develop during sample preparation. These effects were minimized by sampling the largest practical area for analysis and by rejecting samples which showed, through visual inspection, obviously non-uniform contact distributions. All results presented here are derived from 25- frame mosaics which represent about 11% of the total surface area. Over 1000 images were analysed for prepara-

tion of this report. A task of this magnitude is manageable because image analysis is largely automated once the processing parameters are determined. Below we show that the frequency distributions of contact sizes are insensitive to normal stress or other experimental variables. Hence, the variability from limited sampling of the surfaces primarily affects determinations of net contact area and mean contact stress.

In each material, contact creep was observed to increase the area of contact by the logarithm of elapsed time. All image data used in this report were collected only after a contact time of 1000 seconds had elapsed at a fixed normal stress. By this time the creep process had slowed to a negligible rate relative to the time required to collect the 25 frame mosaic.

### 3. Image deconvolution

We have refined the procedure of Dieterich and Kilgore (1994) to address systematic errors and resolution losses inherent to the optical system. To improve the quality of the images, they are processed by performing a deconvolution prior to analysis to remove undesirable optical effects which we have quantified. Scattering originates from theoretically imposed limits of image resolution as well as non-ideal response of the optical system. These reduce recorded light intensity within a contact by an amount that is determined by the distance from the contact boundary and by the shape of the boundary. For small contacts, peak light intensity will be less than that of larger contacts. The net result is loss of contact detail and impaired detection of small contacts following separation of an image into regions of only black or white at a threshold light intensity.

The response of the optical system was quantified using commercially available precision pinholes which represent idealized contacts with known input signal intensity and known dimensions. Images of pinholes with diameters of 2 μm, 5 μm, 13 μm and 31 μm were analysed. The setup and optical path used to image the pinholes was identical to that employed for the surface contact observations. Stainless-steel sheets, 0.012 mm thick, containing the pinholes were placed between the two surfaces which would otherwise be in contact. The roughened sur-

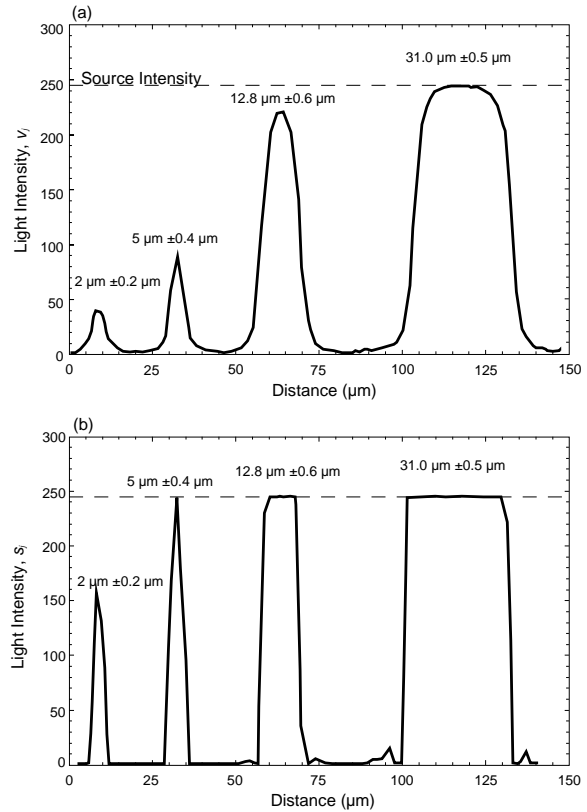


Fig. 3. Profiles of light intensity across images of precision circular pinholes. (a) Unprocessed image. (b) Deconvolved image. The dashed line indicates the light intensity striking the pinholes.

faces were replaced by polished surfaces to insure the pinholes were uniformly illuminated at a known intensity. Fig. 3a shows profiles of light intensity across the pinholes from the digitized images. Note the reduced intensity near the edges of the large pinholes and progressive reduction of peak intensity with pinhole diameter.

The recorded digital image is represented as the convolution, of a signal (the light transmitted across the contacting surfaces) and the response function of the optical system:

$$v_i = \sum_{j=l}^n G_{ij} s_j \tag{1}$$

where  $v_i$  is the recorded intensity at pixel  $i$ ,  $s_j$  are signal intensities at pixels  $j$  and the kernel  $G_{ij}$  is the response function. In practice, because scattering principally affects a limited region, the summation over  $j$  is restricted to pixels in the vicinity of  $i$ . The

goal of the image processing is to solve for the signal intensities  $s_j$  given the observed intensities  $v_i$  and the response function. The pinhole image data provide the basis for estimation of the response function  $G_{ij}$  because the input signal  $s_i$  and the recorded signal  $v_i$  are both known. Through trial and error modeling of the pinhole data, we find that the sum of two modified Gaussian distributions provides an adequate empirical description of  $G_{ij}$  :

$$G_{ij} = \frac{c_1}{2\pi b_1^2} \exp\left[\left(\frac{-r_{ij}^2}{2b_1^2}\right)\right] + \frac{c_2}{2\pi b_2^2} \exp\left[\left(\frac{-r_{ij}^2}{2b_2^2}\right)\right]$$

where  $r_{ij}$  is the distance (in pixel units) from the center of pixel  $i$  to the center of pixel  $j$ . The constants  $b_1$ ,  $b_2$ ,  $c_1$  and  $c_2$  were obtained by modeling of the pinhole profile data using Eqs. 1 and 2. For the images reported here  $b_1$  and  $b_2$  are 0.40 and 1.40, respectively, and the scaling constants  $c_1$  and  $c_2$  are 0.08 and 0.92 respectively.

Fig. 3b gives profiles of light intensity across the pinhole images following deconvolution of Eq. 2 for signal intensities  $s_i$ . We employed an iterative method (Young's over-relaxation) to solve for  $s_i$ . An added condition is imposed during processing which limits the maximum permitted intensity which is based on the recorded intensity of the illumination. This results in flat intensity profiles within the larger pinhole images. Note that deconvolution steepens the intensity gradients at the edges of the pinholes, which improves definition of edges and restores image intensity for the small pinholes. The intensity of the 2  $\mu\text{m}$  diameter pinhole is less than source illumination because it does not align perfectly with the camera pixels and because the image area of the pinhole is less than one square pixel.

Some benefits of the deconvolution are illustrated by the pinhole data of Fig. 3. In the unprocessed raw images, a threshold intensity appropriate to properly resolve the size of the large pinholes would be above the detection threshold for the small pinholes. Similarly, a threshold intensity that resolves the smallest pinhole would yield oversized images for the larger pinholes. Deconvolution reduces the sensitivity of the apparent pinhole diameter on threshold level and registers the smallest pinholes for a range of threshold levels acceptable to properly resolve the size of the large pinholes. Tests were carried out with im-

ages of microscope resolution targets. Those tests show that the deconvolution procedure brings out details that could not be resolved in the unprocessed images at a threshold light intensity, and verify that spurious features are not introduced by the deconvolution procedure which would systematically affect the contact area measurements.

Fig. 4 shows a detail of a contact image before and after deconvolution. The processing appears to be effective in bringing out features that could be discerned in direct visual observation through the microscope, but which are lost in the thresholded unprocessed images. When compared to the unprocessed images, the deconvolved images show small contacts that could not be delineated at intensity thresholds suitable for larger contacts and improved detail of contact geometry.

Threshold light intensity levels used to render the regions of contact in the deconvolved images were based on comparisons of the video images with direct visual observations. Generally the threshold intensity that was employed was about 0.65 of the peak intensity observed in larger contact regions. From repeated direct visual examination of contacts through the microscope (by both of us) we estimate that our uncertainty in being able to estimate the correct threshold level is about  $\pm 0.06$  of the peak intensity (one standard deviation). The resultant uncertainty in actual contact area varies inversely with contact area. For the data reported below, uncertainties from this source vary from  $\pm 0.07$  to  $\pm 0.5$  of the contact area.

Fig. 5 shows distributions of contact areas for a 25 frame mosaic before and after deconvolution and illustrates their sensitivity to the threshold level employed to render the contacts. The heavy lines give the distributions obtained for the deconvolved images using seven different threshold levels centered on the preferred value and separated by increments of 0.02 times the peak intensity. The light lines similarly give the contact distributions for the raw image data. Relative to the distributions from the processed images the raw image data show marked depletion of the number of contacts with areas less than about 100  $\mu\text{m}^2$  (approximate contact diameter of about 10  $\mu\text{m}$ ). This is consistent with the pinhole data which indicate that contacts with diameters of 10  $\mu\text{m}$  or less, will be under-represented in the raw

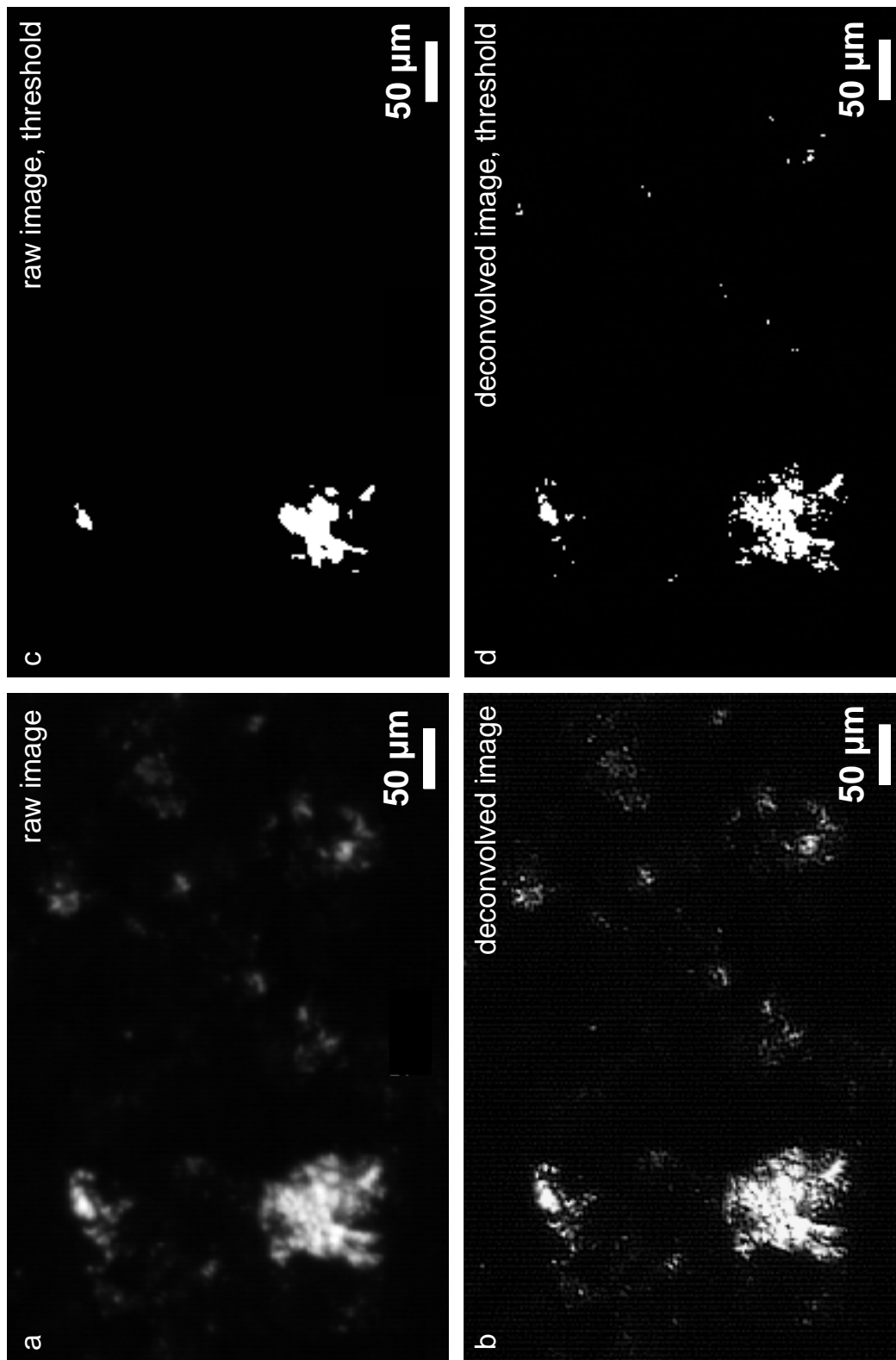


Fig. 4. Detail of contact image of quartz lapped with #60 abrasive at 30 MPa normal stress. (a, b) Grey scale images before and after deconvolution, respectively. The rendering of contacts by a threshold intensity is shown in (c) and (d) before and after deconvolution, respectively.

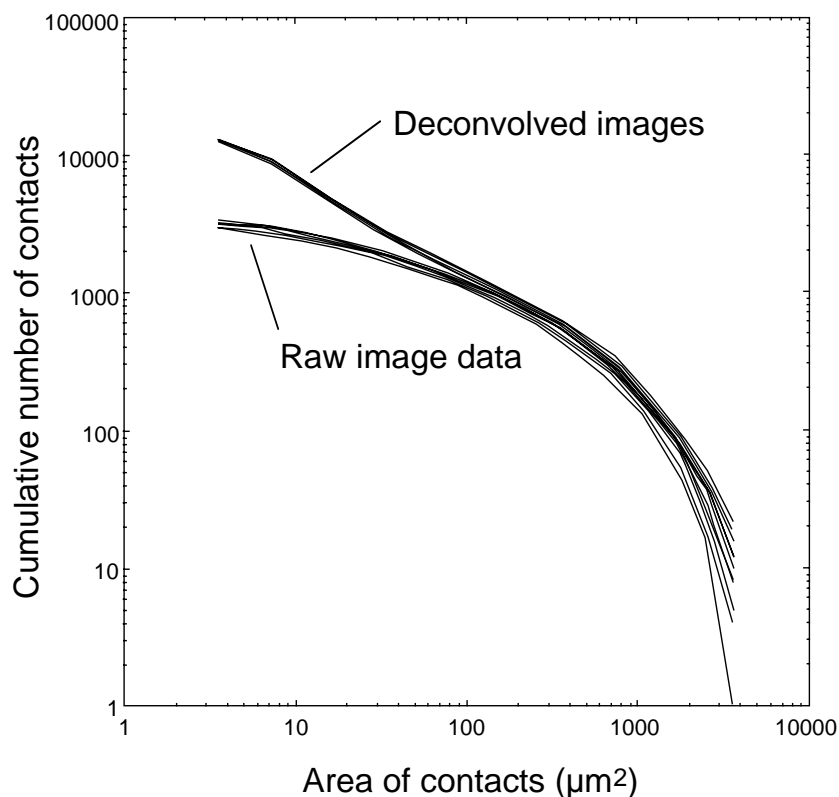


Fig. 5. Example distributions (acrylic plastic with #60 surface at 16 MPa) of cumulative number of contacts equal to or larger than the indicated area. The distributions before processing are shown by thin lines and the distributions following deconvolution are shown by heavy lines. In each case seven different threshold levels were employed to delineate the contacts, centered on the preferred threshold level. The distributions for the processed images overlap

images. In addition, the distributions obtained with the seven different threshold levels are more closely clustered following processing. We conclude the shapes of the frequency distributions are insensitive to uncertainty of the threshold light intensity used to delineate contact regions.

#### 4. Results

Representative images of the four materials studied are shown in Fig. 6. The contacts generally have rather convoluted shapes and tend to cluster into groupings with larger contacts surrounded by smaller satellite contacts. In each material the area of contact represents a small fraction of the total surface, which indicates the stresses supported by the contacts are high. For acrylic samples (Fig. 6a) contacts have well defined, though convoluted, edges. The calcite

samples (Fig. 6b) yielded poorer image quality than the other materials. The poor image quality may be the cause of the more rounded and less distinct contact boundaries seen in the calcite. We believe the reduced image quality in calcite is due to its very high birefringence combined with rather thick wafers. Although the wafers were oriented perpendicular to the *c*-axis of calcite, double refraction effects could be discerned, which perhaps originated from mechanical twinning in the region of the contacts. For the glass and quartz samples (Fig. 6c and 6d, respectively) the contacts are often very angular, appearing to consist of fractured fragments of material and are cut by linear features which appear to be cracks.

Light transmission across contacts is variable and somewhat less than that of polished surfaces of the intact material. This appears to indicate transmissive loss at the contacts or within the material in the vicinity of the contacts. Causes for the reduced light

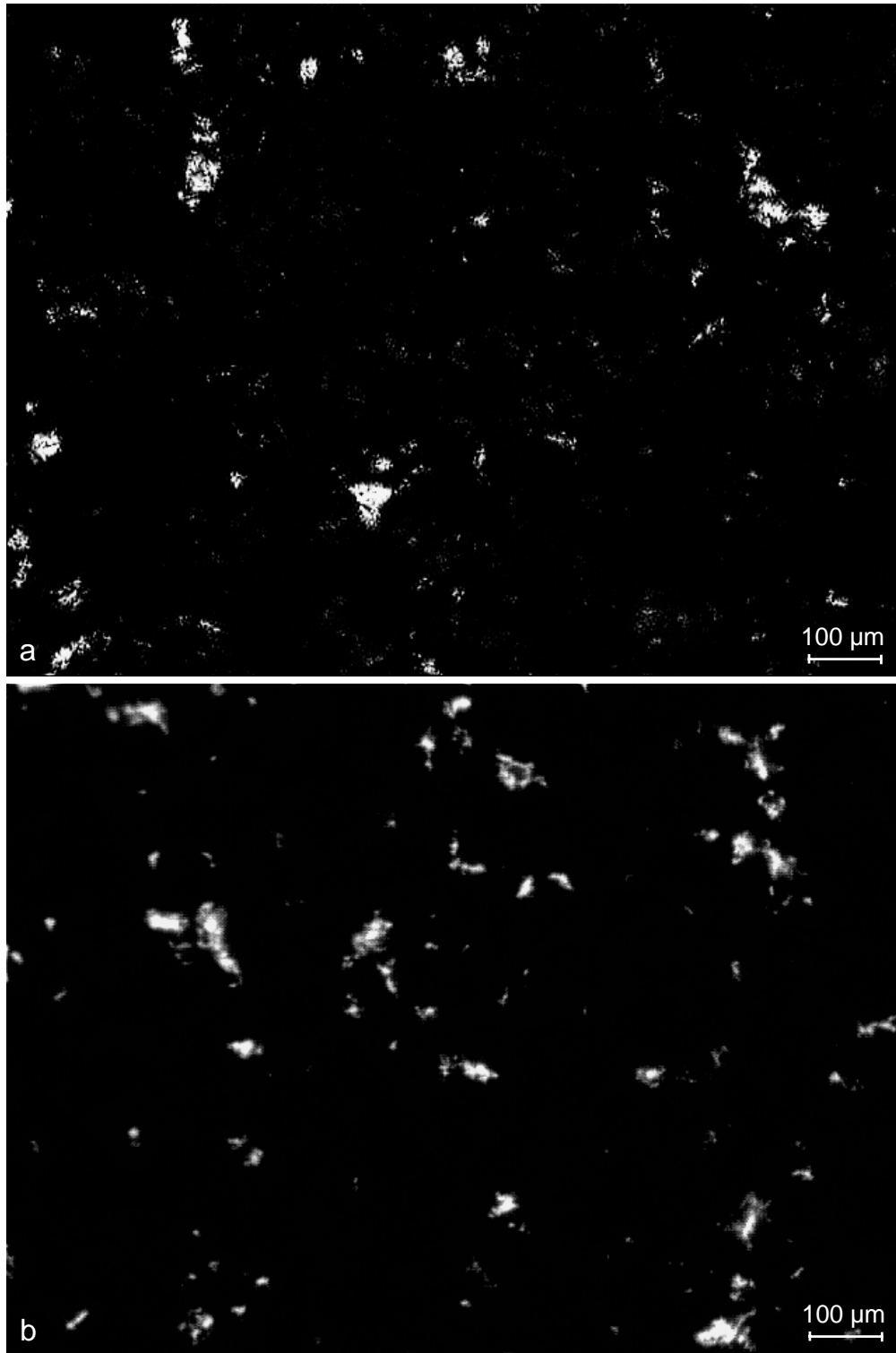


Fig. 6. Representative contact images (deconvolved) #60 acrylic at 4 MPa (a), #240 calcite at 30 MPa (b), #60 soda-lime glass at 20 MPa (c) and #60 quartz at 30 MPa (d).

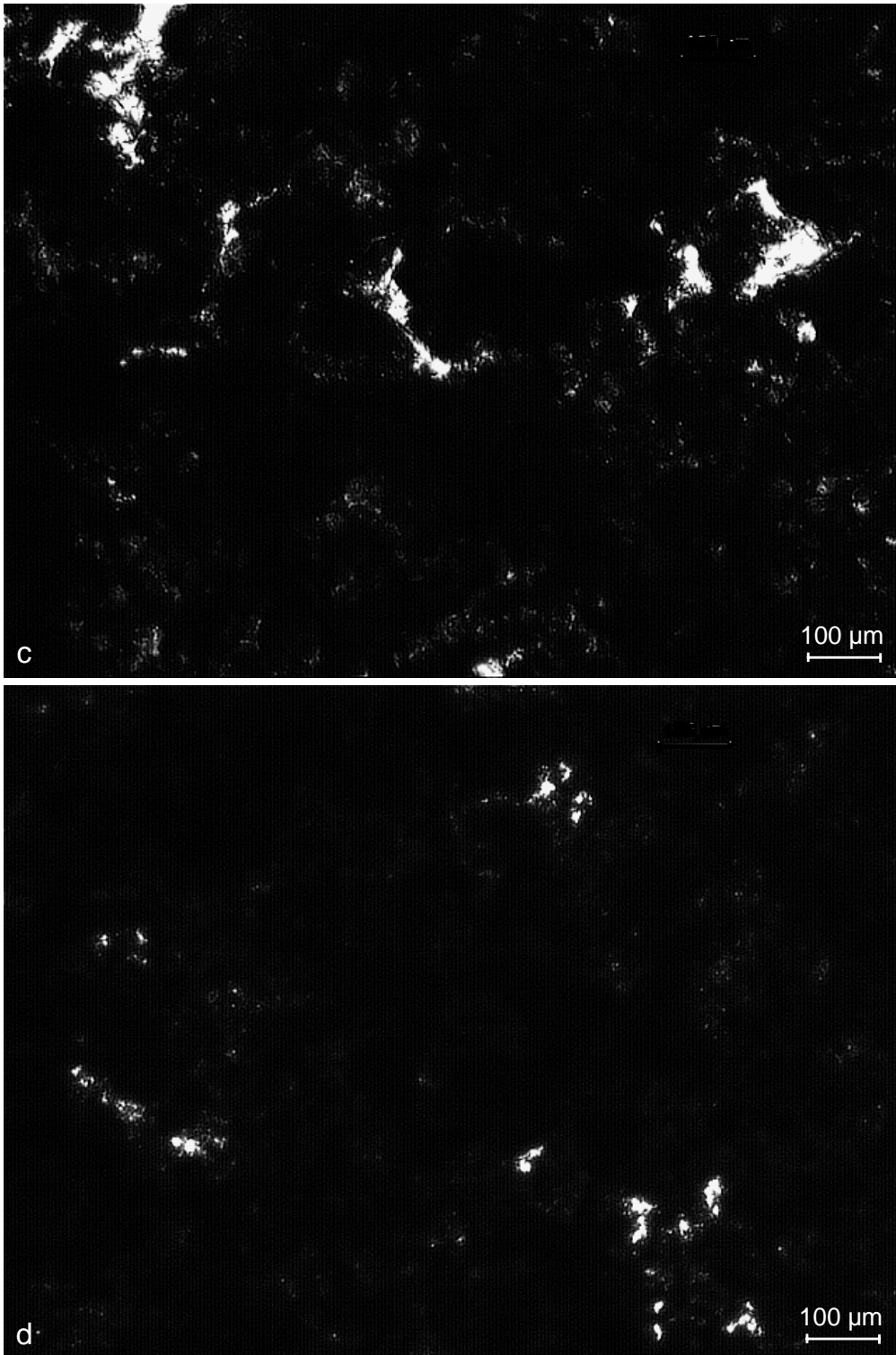


Fig. 6. (continued).

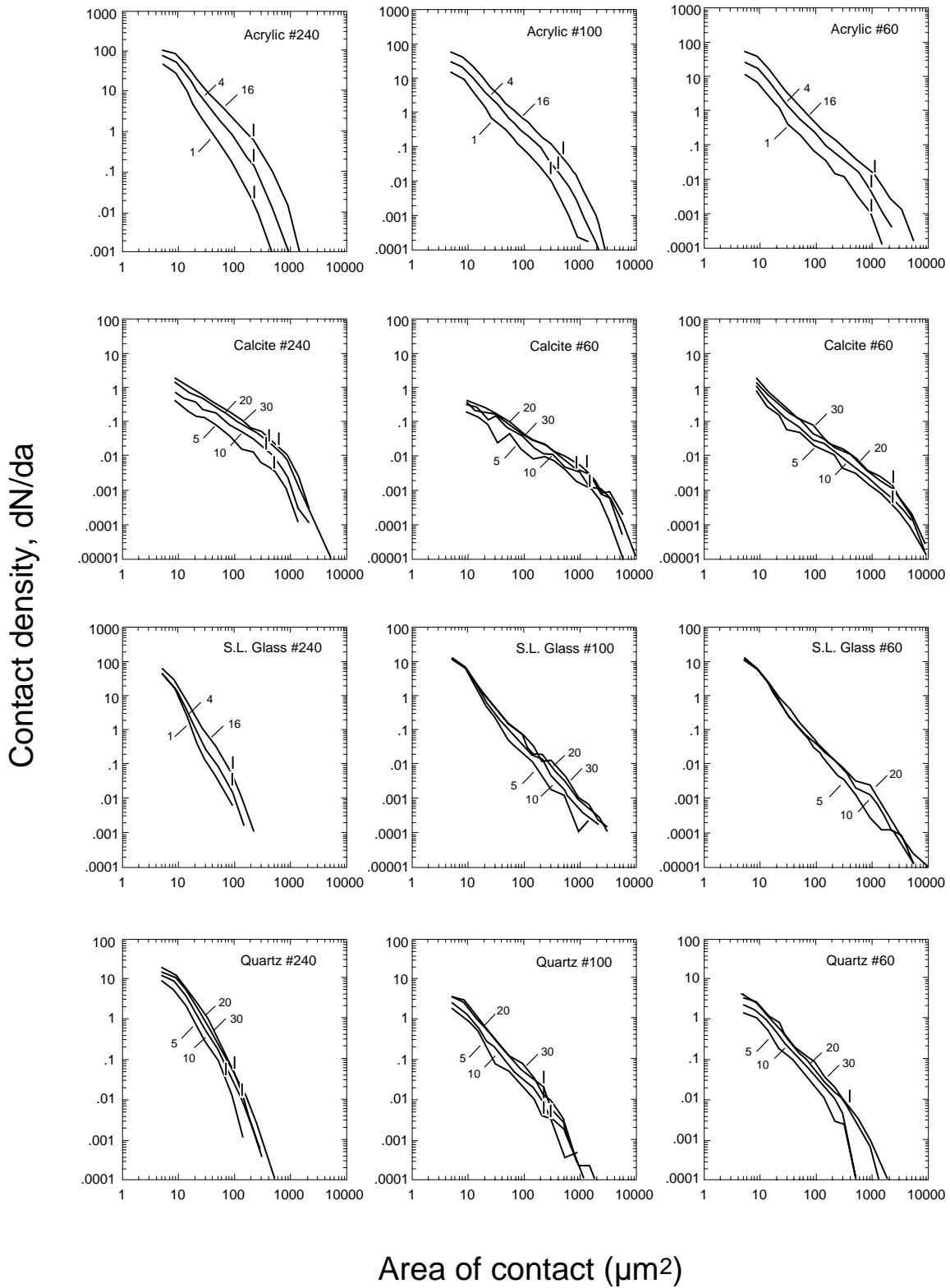
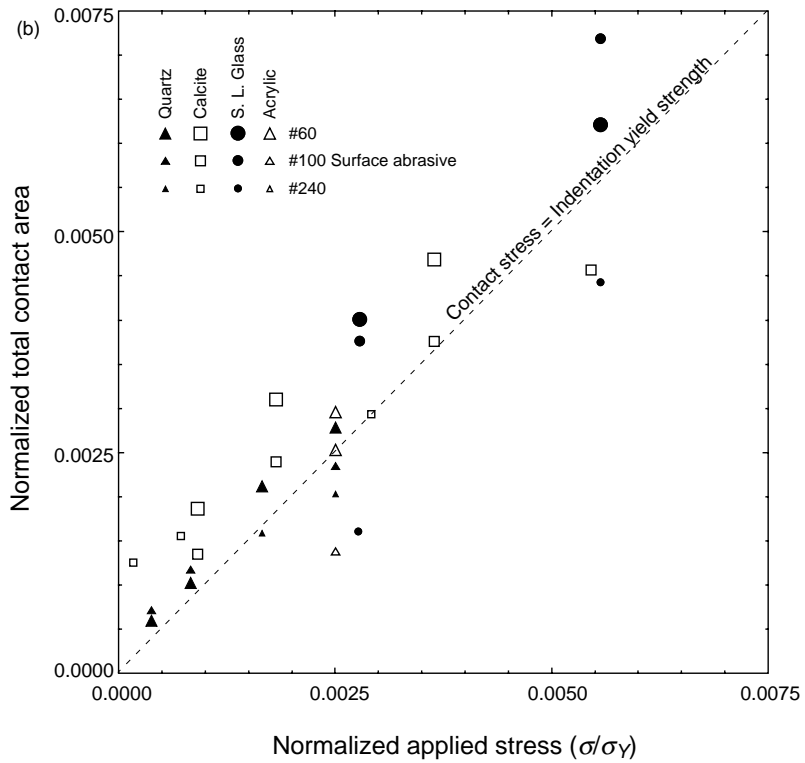
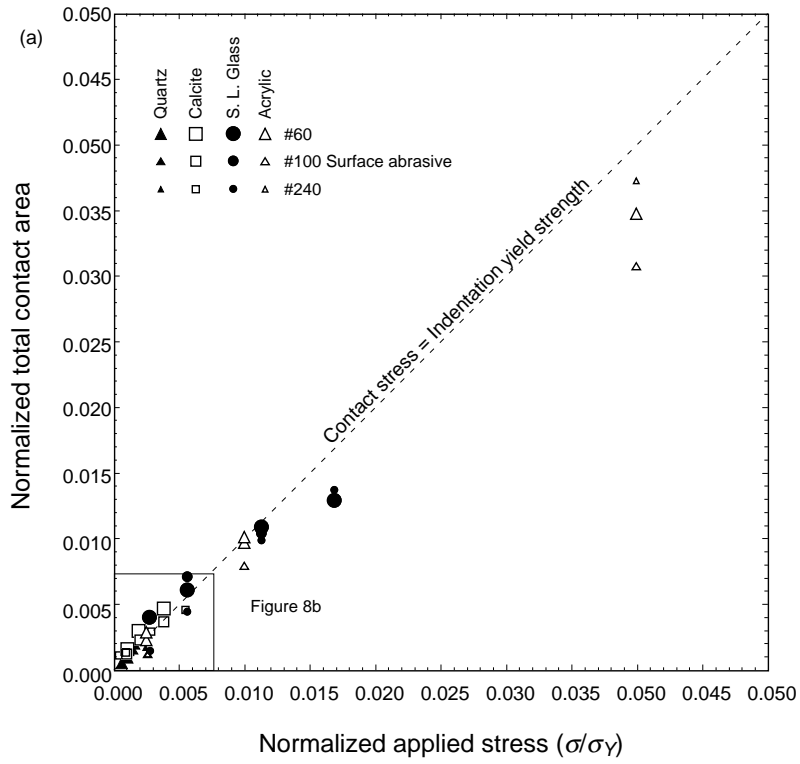


Table 1

Material	Surface preparation	Normal stress (MPa)	Contact size distribution		Mean contact stress (MPa)
			$D$	$a_L(\mu\text{m}^2)$	
Acrylic	240	1	2.28	210	430 ± 170
Acrylic	240	4	1.87	210	500 ± 100
Acrylic	240	16	1.55	210	730 ± 80
Acrylic	100	1	1.87	300	340 ± 50
Acrylic	100	4	1.75	400	390 ± 50
Acrylic	100	16	1.65	500	520 ± 60
Acrylic	60	1	1.80	910	400 ± 60
Acrylic	60	4	1.68	910	400 ± 50
Acrylic	60	16	1.60	1000	460 ± 50
Calcite	240	5	1.18	520	3110 ± 840
Calcite	240	10	1.09	370	2260 ± 480
Calcite	240	20	1.06	370	1980 ± 450
Calcite	240	30	1.08	400	2210 ± 480
Calcite	100	5	1.08	1500	1330 ± 310
Calcite	100	10	1.08	900	1390 ± 300
Calcite	100	20	1.05	1200	1910 ± 350
Calcite	100	30	1.05	1200	2290 ± 410
Calcite	60	5	1.30	2600	1250 ± 260
Calcite	60	10	1.29	2600	1610 ± 330
Calcite	60	20	1.24	2600	1840 ± 390
Calcite	60	30	1.24	2200	2310 ± 490
Glass	240	1	(3.38)	-	820 ± 420
Glass	240	4	2.69	(90)	2620 ± 1220
Glass	240	16	2.62	(90)	5500 ± 2010
Glass	100	5	2.13	-	3760 ± 610
Glass	100	10	1.98	-	4202 ± 420
Glass	100	20	1.78	-	5300 ± 450
Glass	100	30	1.78	-	6550 ± 560
Glass	60	5	2.07	-	2670 ± 430
Glass	60	10	1.91	-	3220 ± 430
Glass	60	20	1.76	-	4240 ± 500
Quartz	240	5	2.67	(90)	9170 ± 2270
Quartz	240	10	2.64	150	9440 ± 2120
Quartz	240	20	2.45	100	12600 ± 2740
Quartz	240	30	2.38	100	14870 ± 3150
Quartz	100	5	1.67	300	7510 ± 650
Quartz	100	10	1.60	210	8510 ± 670
Quartz	100	20	1.67	210	9500 ± 760
Quartz	100	30	1.62	210	12810 ± 890
Quartz	60	5	1.55	-	8640 ± 1120
Quartz	60	10	1.55	-	9940 ± 1100
Quartz	60	20	1.55	400	9380 ± 1080
Quartz	60	30	1.55	400	10820 ± 810

Poorly determined value between brackets.

Fig. 7. Density distributions by area of the contacts, scaled to a 1 mm x 1 mm surface. The short vertical lines indicate the limits  $a_L$  for power law behavior which are listed in Table 1.



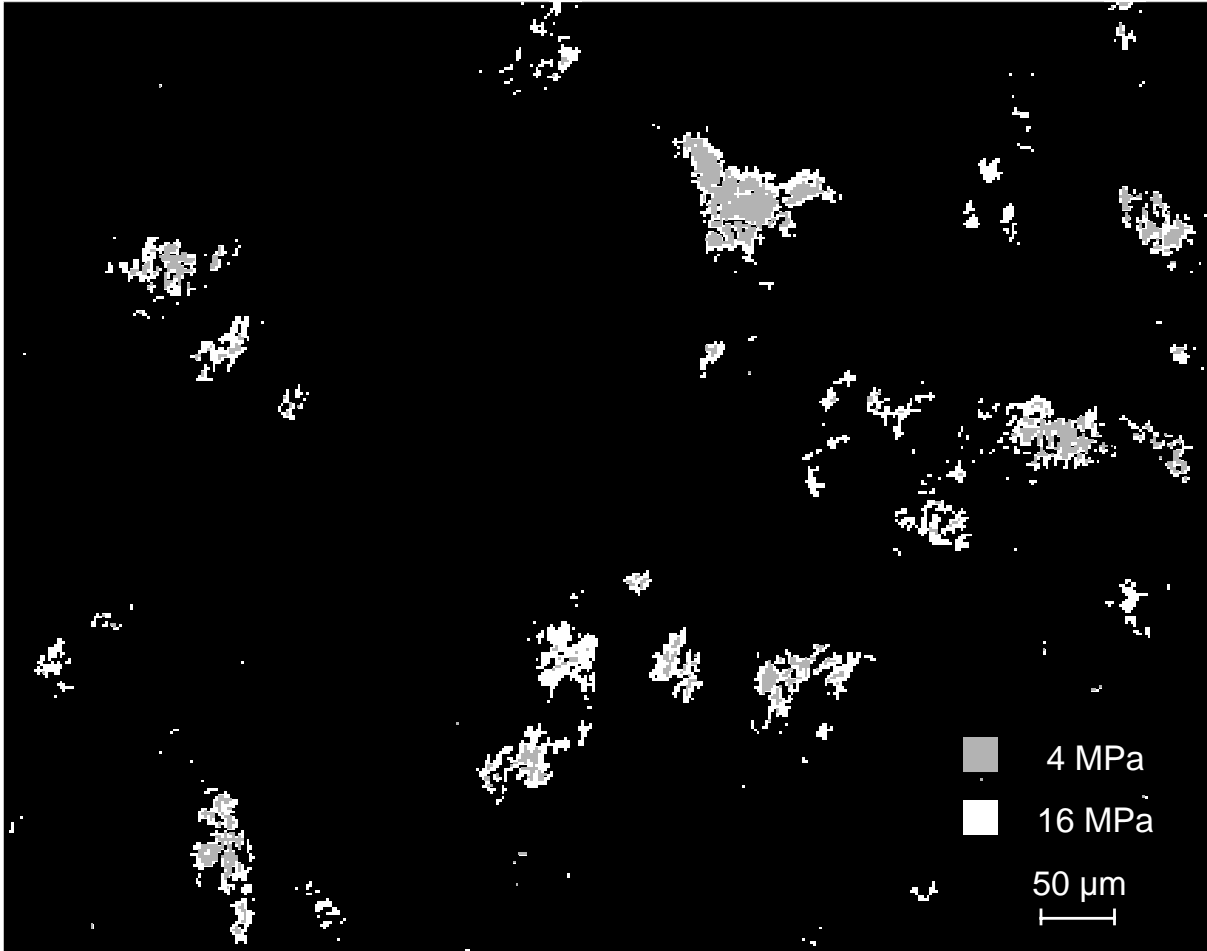


Fig. 9. Superimposed images at 4 and 16 MPa normal stress from #60 surface of acrylic, showing characteristics of contact growth as normal stress is increased.

transmission are not known, but we speculate it is due to scattering either by damage such as microcracking around the contacts or by small voids within the contact interface that are too small to resolve optically.

Over a range of contact sizes, the density distribution of contact area are described by a power law:

$$\frac{dN}{da} \equiv \rho = Ca^{-D} \quad (3)$$

where  $N$  is number of contacts,  $a$  is normalized area

of the contacts (contact area/total surface area) and  $C$  and  $D$  are constants. The distributions of  $\rho$  for each material, surface preparation and nominal normal stress are shown in Fig. 7. With the possible exception of soda-lime glass, significant departures from Eq. 3 occur above a limiting contact area designated as  $a_L$  ( $\mu\text{m}^2$ ). See Table 1 for tabulations of  $D$  and  $a_L$ . The contact density distributions roll off at  $3.5 \mu\text{m}^2$  (one square pixel). This is expected because contacts comparable in size to a pixel will often fail to align with the camera pixels and conse-

Fig. 8. Normalized total contact area (total area of contact/surface area) against normalized applied stress (applied normal stress/indentation strength). Points falling on the dashed line, which has a slope of one, have a mean contact stress equal to the indentation strength; (b) shows detail of dense cluster of points from (a).

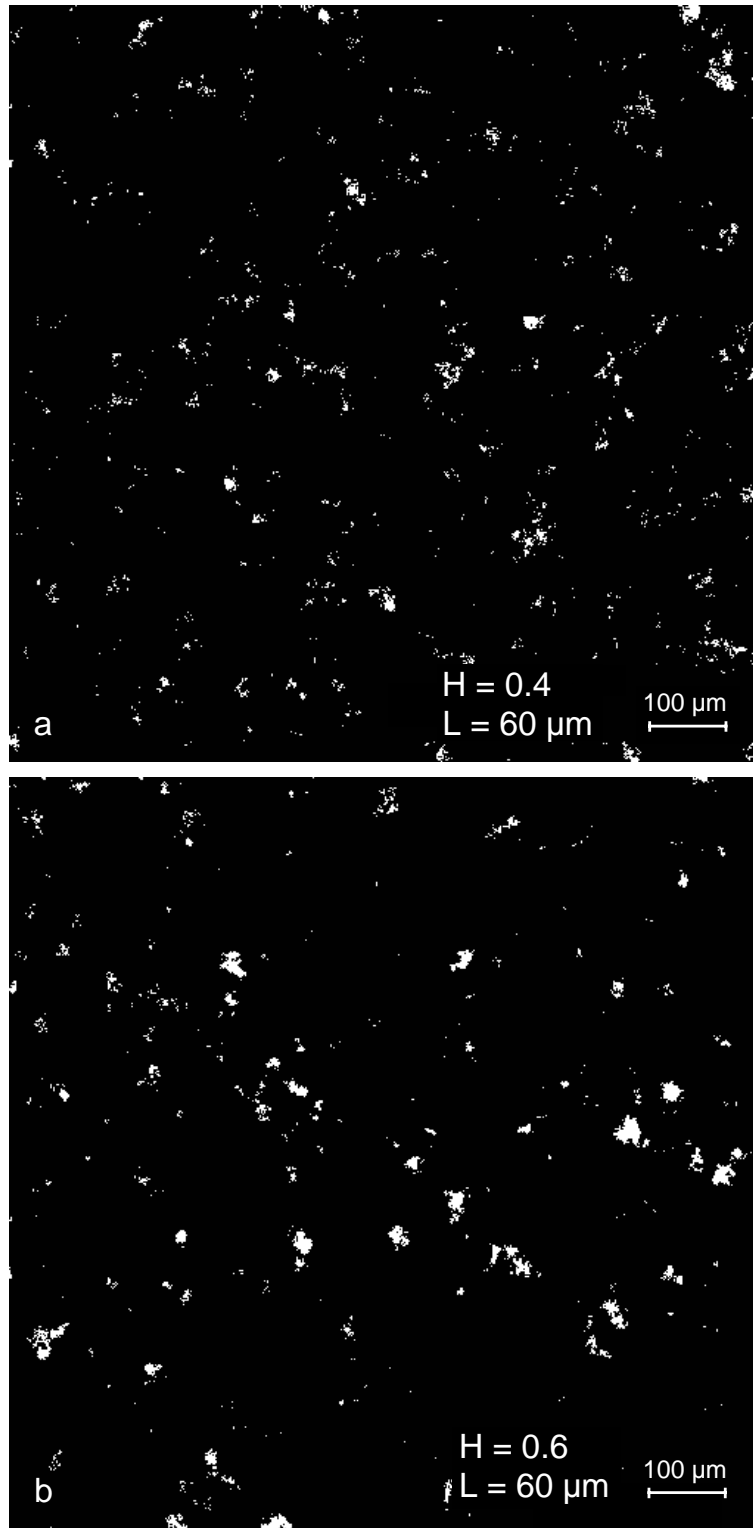


Fig. 10. Synthetic contact images. Values of the Hurst exponent ( $H$ ) and the limiting length scales ( $L$ ) used to generate these fractal surfaces are indicated in each image.

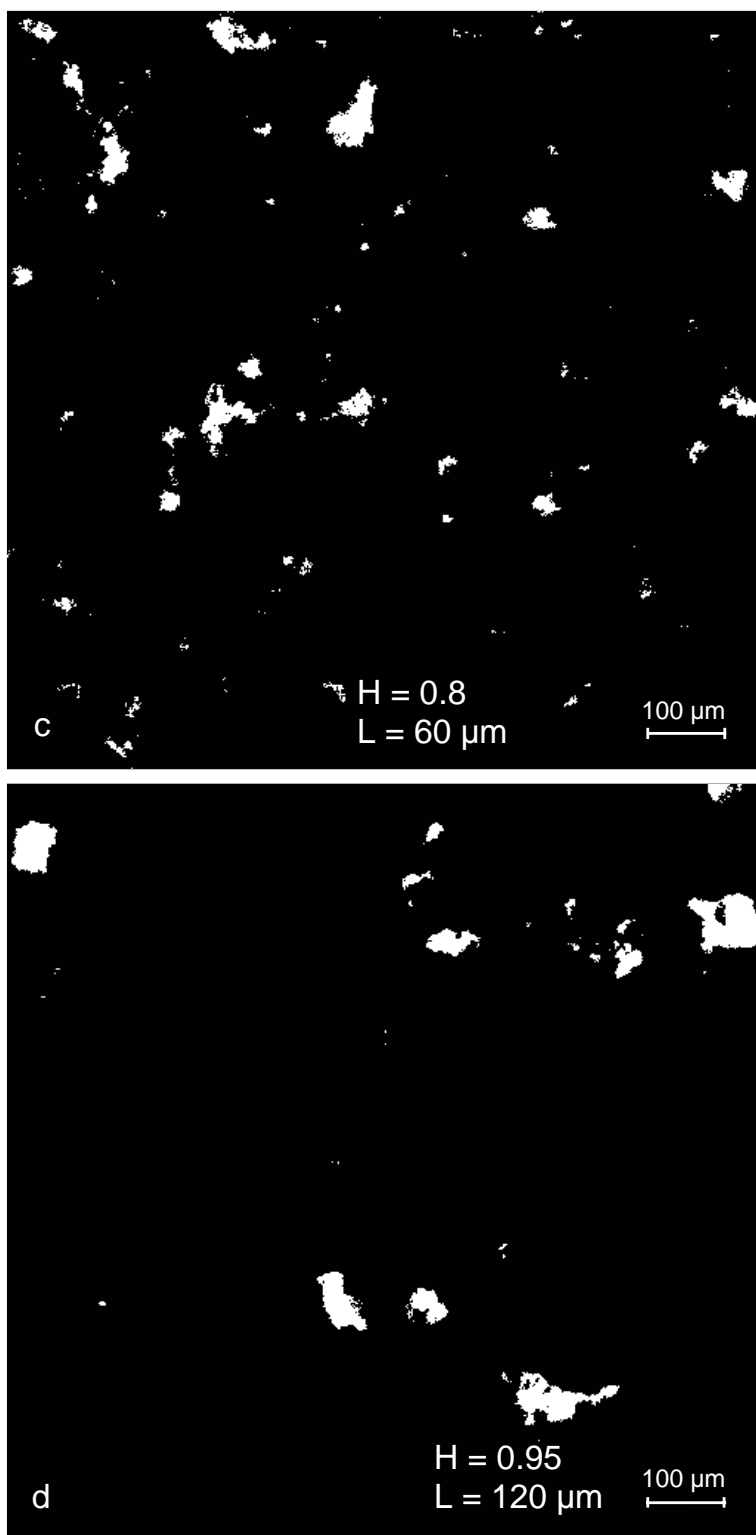


Fig. 10. (continued).

quently will be recorded by several pixels with resulting loss of intensity. From Table 1 and Fig. 7, the limiting size  $a_L$  for power law behavior evidently correlates with the size of abrasive grit used to lap the surfaces.

The power law distribution is the defining characteristic of a fractal distribution and the exponent  $D$  is the fractal dimension (Turcotte, 1989). Integration of Eq. 3 gives the cumulative number of contacts equal to or greater than  $a$ , which is also a power law with exponent  $(-D + 1)$ . We prefer the density distribution over the cumulative distribution because it better defines  $a_L$ . For the contact area distributions determined in this study,  $D$  varies from about 1.05 to 3 depending on material, normal stress and surface roughness. Below, we describe a simple geometric model of the contact process which accounts for several characteristics of the distributions.

With each material that was studied, the actual area of contact was found to increase in a roughly linear manner with the applied normal stress (Fig. 8). To facilitate comparisons of the different materials in Fig. 8, the normalized contact area  $a_T$  (total contact area/total surface area) is plotted against normalized applied stress ( $s/s_y$ ), where  $s_y$  is the microindentation yield strength. The data show considerable scatter, but cluster near a line with slope equal to one (dashed line in Fig. 8), which indicates that the mean contact stress approximates the indentation strength of each material. Indentation yield stresses employed for this purpose are 400 MPa for acrylic (Dieterich and Kilgore, 1994), 1800 MPa for calcite (Westerbrook and Jorgensen, 1969; Wakeman et al., 1993), 5500 MPa for soda-lime glass (Marsh, 1964; Lawn et al., 1980; Dieterich and Kilgore, 1994), and 12,000 MPa for quartz (Brace, 1963; Westerbrook and Jorgensen, 1968; Ferguson et al., 1987).

Mean contact stresses, listed in Table 1, are obtained directly from the total contact area and normal stress:

$$\sigma_c = \sigma / \sigma_T \quad (4)$$

where  $\sigma_c$  is mean contact stress,  $a$  is applied normal stress and  $\sigma_T$  is the total contact area/surface area. The  $\sigma_c$  uncertainties in Table 1 represent only the estimated human error of  $\pm 0.06$  in threshold light intensity used to define the contacts. Other sources of error, especially that caused by incom-

plete sampling of spatially non-uniform contact populations, may significantly add to the total uncertainty.

Contact yielding is further indicated by observations of time-dependent increases of contact area at constant applied normal stress. Previously Dieterich and Kilgore (1994) established for acrylic and soda-lime glass that time-dependent increases of contact area quantitatively agree with the area increases that occur from microindentation creep. A paper describing details of contact creep with calcite and quartz is in preparation. In brief, these experiments show, for each material, that contact creep increases the area of contact by the logarithm of contact time. The time-dependent increases of contact area occur at all normal stresses. However, the contact stress data (Table 1), though highly scattered, show a tendency for the contact stresses to be less than the indentation strength of the materials at the lower applied normal stresses. This suggests, that many contacts, or portions of contacts, in the contact populations are below the yield stress. Contact yielding in addition to elastic contact deformation has been previously inferred by Brown and Scholz (1986) for marble and by Yoshioka (1994b) based on theoretical modeling. We conclude that contact yielding is an important mechanism of contact deformation in each of the materials examined.

In our previous study (Dieterich and Kilgore, 1994) we observed, through comparisons of successive video images as normal stress is increased, that three processes contribute to increase of surface area. They are: (1) enlargement of individual contacts, (2) coalescence of neighboring contacts, and (3) appearance of new contacts. The deconvolved images from this study show these processes operate in each material and surface preparation we have tested. Fig. 9 shows an example of superimposed images of a region taken at two different normal stresses.

## 5. Model of contact distributions

Natural and artificially prepared surfaces have fractal topographies as characterized by power law dependence of surface roughness on spatial wavelength (Brown and Scholz, 1985a, Brown and Scholz,

1985b; Power et al., 1988; Yoshioka, 1994a, Yoshioka, 1994b). This suggests a possible geometric relationship between surface topography and the observed power law distributions of contact frequency against contact size. This possibility is reinforced by two additional observations. First, the contact images are similar in appearance to pictures of fractal islands and coastlines formed from random fractal topographies (Mandelbrot, 1983). Second, the breakdown of the power law contact area distributions at length scales which correlate with the size of the abrasive grit used to lap the surfaces appears to be comparable to the long-wavelength breakdown of fractal surfaces topographies also seen for ground surfaces (Brown and Scholz, 1985a; Yoshioka, 1994b). We have investigated the origins of the contact area distributions and their possible relationship to fractal surface topography through a simple numerical simulation of the contact process.

The analysis is based upon numerical models of

surfaces with random fractal topographies. We use the method of random mid-point displacement (Pietgen et al., 1992) to create the model fractal surfaces. The surface is created on a square grid with dimensions of 513 x 513. The grid points correspond to pixels in the simulated images. The controlling parameter for specifying the fractal surface topography is the Hurst exponent  $H$  which has values in the range 0 to 1. Decreasing  $H$  increases the 'sharpness' of the surface topography and a value of  $H = 0.5$  corresponds to a Brownian surface. See any standard reference (for example, Pietgen et al., 1992) for further discussion of random fractal topographies. In creating the simulated surface topographies a limiting spatial wavelength  $L$ , was employed. Topography at wavelengths in excess of  $L$  was attenuated to simulate the observed cutoff in the power spectral amplitudes of topographies measured for ground surfaces (Brown and Scholz, 1985a; Yoshioka, 1994b).

The objective of the simulation is to map the

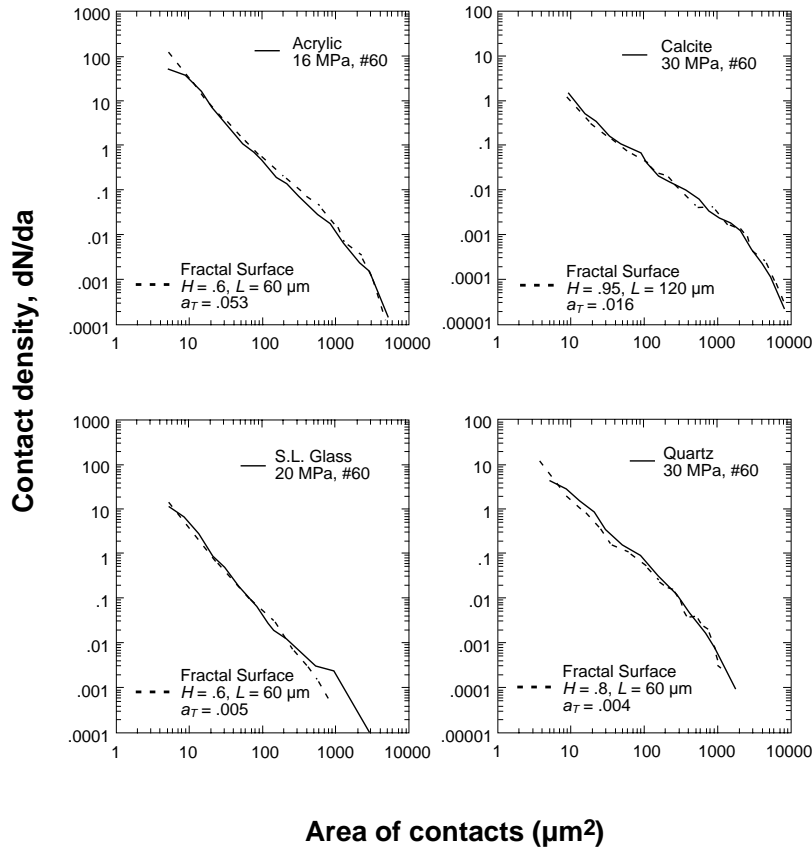


Fig. 11. Examples comparing contact area distributions from simulated surface images (dashed lines) with distributions from experiments.

regions of contact that develop as the two simulated surfaces are brought together. The contact process is represented by the simple expedient of removing material at regions where the irregular surfaces overlap. The effects of normal stress and material yield strength are simulated by adjusting the amount of closure between the surfaces to balance the average contact stress to the indentation strength. Hence, this simulation procedure is essentially geometric and ignores details of the deformation process at regions of contact.

To carry out the simulations, an equivalent procedure is employed which significantly simplifies the computations. The separation between the surfaces is converted into a single composite topography (Brown and Scholz, 1985a) by taking the sum of the heights of the two surfaces at each point. The problem then is equivalent to pressing the composite topography against a rigid flat surface. Regions of contact in the simulation are then mapped by taking slices through

the fractal topography at elevations which correspond to the location of the flat surface. The procedure of mapping regions defined by an elevation makes this problem equivalent to the classic fractal coastline problem. Reductions of contact elevation correspond to closure of the surfaces under the action of increasing normal stress. Synthetic contact images created by this procedure were analysed using the image analysis software employed analysis of the real contact images.

Fig. 10 shows synthetic contact images for several simulated fractal surface topographies obtained by this procedure. Comparisons of the simulated and real contact images disclose several similarities which include complex contact shapes, clustering of smaller contacts around large contacts and a correlation between contact size and surface roughness. Furthermore, the contact area distributions can be modeled in detail by the synthetic contact images (Fig. 11). The model distributions shown in Fig. 11 are each

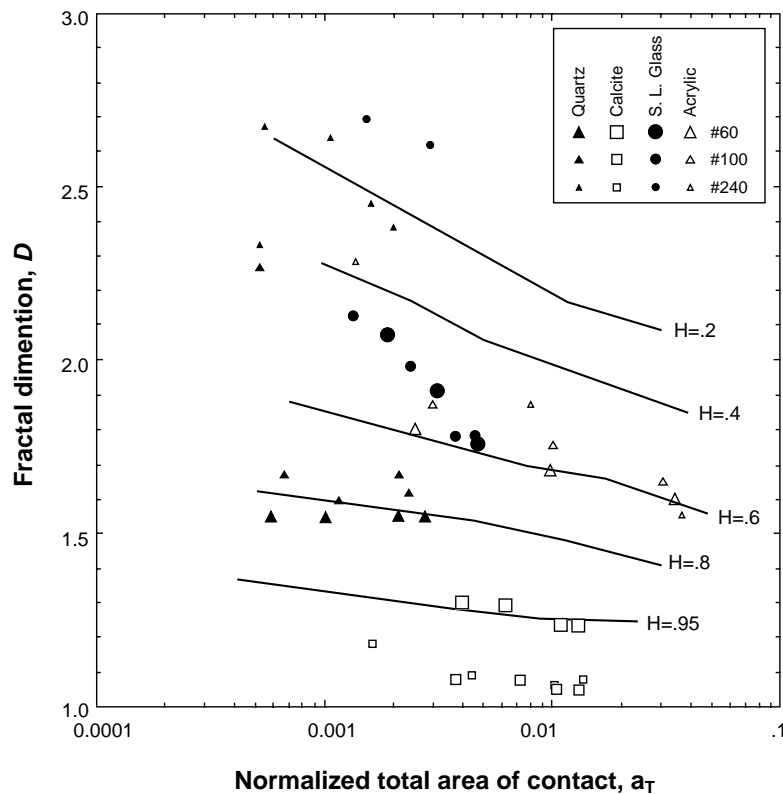


Fig. 12. Power law exponent  $D$  against normalized total contact area from experiments and from simulations. All simulations assume  $L = 60 \mu\text{m}$ .

derived from 20 synthetic images. In the fractal surface simulations the size limit,  $a_L$ , of power law scaling appears to be insensitive to  $H$  or to normalized contact area (over the limited range of contact areas simulated) and is related to  $L$  roughly as:

$$a_L \approx 0.2 L^2 \quad (5)$$

For surfaces prepared with the same abrasive grit, the experimental data for quartz, calcite and acrylic indicate that  $a_L$  varies inversely with hardness. This may reflect more effective abrasion of softer materials which creates larger topographic features. Glass is an exception and does not have a well defined  $a_L$ . The exponent  $D$  in the power law distributions depends on the scaling exponent  $H$  used to generate the surface topography (Fig. 12). As the sharpness of the topography increases (decreasing  $H$ ) the frequency of small contacts is enhanced relative to large contacts resulting in larger  $D$ . The rather weak dependence of the distributions on normal stress indicates a roughly self-similar growth of contact area with increasing normal stress. The enlargement and coalescence of existing contacts is approximately balanced by the appearance of small new contacts.

In detail however, the growth of contact area is not strictly self-similar. In the experiments, as well as the simulations,  $D$  systematically decreases as the total area of contact increases. In the fractal surface simulations contact area is a surrogate for normal stress. Hence, as total area of contact increases there is progressive increase in the numbers of larger contacts relative to small contacts. We believe this effect arises for two reasons. First, the surfaces are flat at long wavelengths (above the scaling cutoff  $L$ ) which promotes the formation of numerous small contacts when the surfaces first begin to touch as opposed to a few large contacts that would form if large wavelength topographic features existed. Only as the surfaces move together, can large contacts form. Second, as noted above (Fig. 9) an important mechanism of area growth is contact coalescence. As the surfaces move together contacts become more closely spaced and formation of large contacts through coalescence occurs at increasing rates resulting, eventually, in a connected contact that spans the entire surface (percolation threshold). Except for glass, the decrease of  $D$  with increasing contact area

(increasing normal stress) observed in the experiments follows paths that have slopes that are similar to the simulations (Fig. 12). The #100 and #60 surfaces of glass show stronger dependence of  $D$  on  $a$  than the simulations. The reasons for the apparent enhanced sensitivity of glass has not been investigated.

## 6. Discussion and conclusions

The imaging method described here provides a rapid means for direct observation of contact processes between roughened surfaces. When a deconvolution is performed to remove known imaging and optical path effects, quantitative data on contact size distributions can be obtained. This observational technique has several advantages over other methods that have been previously employed to investigate contacting surfaces. It provides direct images during an experiment, it is non-invasive and resolution of small contacts is limited only by the theoretical limits of optical systems. In looking ahead at future applications of this procedure it would appear that additional optical measurement techniques could be incorporated. For example, various techniques in use for diamond anvil experiments might be adapted to probe, in detail, the processes that occur in the high pressure and high differential stress environment of individual contacts.

The primary requirement of this approach is that the samples be transparent and of relatively good optical quality. We have demonstrated the feasibility of using thin wafers glued to a transparent substrate, which opens a variety of minerals to study. Also, we have found glass and acrylic plastic to be excellent rock analogs for rate- and state- dependent frictional properties (Dieterich and Kilgore, 1994). Other limitations arise from the requirement for scattering to occur at the non-contacting surfaces in order to distinguish regions of contact from those not in contact. This limits applications to roughened surfaces and large differences in the index of refraction between the samples and the material filling the crack. Consequently, polished surfaces cannot be currently employed, nor can water or other liquids be used to fill the crack during observations. In principle, pressurized gas could be substituted for liquids

to investigate pore pressure effects. Pressure solution and cementation effects in a fluid-filled crack might be imaged by periodically draining a crack while it remains at stress in the apparatus.

The principal observational results of this study are the findings of power law distributions of contact areas for ground surfaces and of contact stresses consistent with the microindentation strength of the materials. Power law scaling arises in a variety of contexts relating to descriptions and analyses of fractures. Nolte et al. (1989) also found power law distributions of contact areas from casts of natural fractures, but at a rather coarser scale of resolution. Fracture and fault topography follow power law scaling (for example, Scholz and Aviles, 1986; Okubo and Aki, 1987; Power et al., 1988) as do fault gouge particle size distributions (Sammis and Biegel, 1989). Gangi (1978) employed an elastic 'bend of nails' model with a power law distribution of asperity heights to characterize crack closure and hydraulic transport properties of cracks and demonstrates equivalence of this model with various representations of contact interactions.

A number of studies (Greenwood and Williamson, 1966; Walsh and Grosenbaugh, 1979; Brown and Scholz, 1985a; Yoshioka, 1994a) employ specific models of contact interactions based on elastic contacts with hemispherical tips. Although these models are successful in reproducing macroscopic characteristics of crack closure, our observations conflict rather fundamentally with the model assumptions of elastic, independent, non-interacting hemispherical contacts. Contact yielding is indicated by our results. In addition, the observations demonstrate highly convoluted contact shapes, clustering of contacts, and contact coalescences as a mechanism of contact area growth, all of which are inconsistent with isolated hemispherical contacts. These observations suggest that contact theories capable of representing contact yielding (Yoshioka, 1994b) and models which statistically relate crack geometry to simple mechanical elements (for example, Gangi, 1978), might be profitably employed for investigation of contact processes.

We are able to reproduce both the appearance of the contact images and the contact area distributions with a simple model based on truncation of random fractal surface topographies. The scaling limit of power law contact area distributions,  $a_L$ , results

from attenuation of the composite surface topography at wavelengths above some value  $L$ . The power law exponent  $D$  of the area distributions is controlled by the 'sharpness' of the composite topography. A fundamental issue in all attempts to understand fracture deformation and fault slip phenomena relates to the scaling of laboratory experiments to natural surfaces. The results of this study show direct relationships between an observable property, composite fracture surface topography, and difficult-to-observe contact properties which include contact area distributions, surface closure and contact stresses.

### Acknowledgements

We thank J. Logan and S. Brown for helpful suggestions in the early phases of the study, and J. Andrews, N. Beeler, and J. Logan for thoughtful reviews. Dieterich wishes to acknowledge and thank Neville Carter who, through instruction and example, instilled a lasting interest in, and appreciation for, experimental rock deformation.

### References

- Brace, W.F., 1963. Behavior of quartz during indentation. *J. Geol.*, 71: 581-595.
- Brown, S.R. and Scholz, C.H., 1985a. Closure of random elastic surfaces in contact. *J. Geophys. Res.*, 90: 5531-5545.
- Brown, S.R. and Scholz, C.H., 1985b. Broad bandwidth study of the topography of natural rock surfaces. *J. Geophys. Res.*, 90: 12,575-12,582.
- Brown, S.R. and Scholz, C.H., 1986. Closure of rock joints. *J. Geophys. Res.*, 91: 4939-4948.
- Carlson, R.L. and Gangi, A.F., 1985. Effect of cracks on the pressure dependence of P wave velocities, I. Crystalline rocks. *J. Geophys. Res.*, 90: 8675-8664.
- Dieterich, J.H. and Kilgore, B.D., 1994. Direct observation of frictional contacts: new insights for state-dependent properties. *Pure Appl. Geophys.*, 143: 283-302.
- Ferguson, C.C., Lloyd, G.E. and Knipe, R.J., 1987. Fracture mechanics and deformation processes in natural quartz: a combined Vickers indentation, SEM, and TEM study. *Can. J. Earth Sci.*, 24: 544-555.
- Gangi, A.F., 1978. Variation of whole and fractured porous rock permeability with confining pressure. *Int. J. Rock Mech. Min. Sci. Geomech. Abstr.*, 15: 249-257.
- Greenwood, J.A. and Williamson, J., 1966. Contact of nominally flat surfaces. *Proc. R. Soc. London, Ser. A*, 295: 300-319.
- Kragelskii, I.N., 1965. *Friction and Wear*. Butterworths, Washington, D.C., 346 pp.

- Lawn, B.R., Evans, A.G. and Marshall, D.B., 1980. Elastic/plastic indentation damage in ceramics: the median/radial crack system. *J. Am. Ceram. Soc.*, 63: 574-580.
- Logan, J.M. and Teufel, L.W., 1986. The effect of normal stress on the real area of contact during frictional sliding in rocks. *Pure Appl. Geophys.*, 124: 471-485.
- Mandelbrot, 1983. *The Fractal Geometry of Nature*, 2nd ed. W.H. Freeman, New York, NY, 460 pp.
- Marsh, D.M., 1964. Plastic flow in glass. *Proc. R. Soc. London, Ser. A.*, 279: 420-435.
- Nolte, D.D., Pyrak-Nolte, L.J. and Cook, N.G.W., 1989. The fractal geometry of flow paths in natural fractures in rock and the approach to percolation. *Pure Appl. Geophys.*, 13 1: 111 - 138.
- Okubo, P.G. and Aki, K., 1987. Fractal geometry in the San Andreas fault system. *J. Geophys. Res.*, 92: 345-355.
- Pietgen, H.-O., Jurgens, H. and Saupe, D., 1992. *Chaos and Fractals, New Frontiers of Science*. Springer-Verlag, New York, NY, 984 pp.
- Power, W.L., Tullis, T.E. and Weeks, J.D., 1988. Roughness and wear during brittle faulting. *J. Geophys. Res.*, 93: 15,268-15,278.
- Sammis, C.G. and Biegel, R.L., 1989. Fractals, fault-gouge, and friction. *Pure Appl. Geophys.*, 131: 253-271.
- Scholz, C.H. and Aviles, C., 1986. The fractal geometry of faults and faulting. In: S. Das, J. Boatwright and C. Scholz (Editors), *Earthquake Source Mechanics*. Am. Geophys. Union, Geophys. Monogr., 37: 147-155.
- Stesky, R.M. and Hannan, S.S., 1987. Growth of contact area between rough surfaces under normal stress. *Geophys. Res. Lett.*, 14: 550-553.
- Turcotte, D.L., 1989. Fractals in geology and geophysics. *Pure Appl. Geophys.*, 131: 171-196.
- Wakeman, R.J., Henshall, J.L. and Carter, G.M., 1993. Solution environment effects on the hardness and toughness of calcite during grinding. *Chem. Eng. Res. Design*, 71: 361-370.
- Walsh, J.B. and Grosenbaugh, M.A., 1979. A new model for analysing the effect of fractures on compressibility. *J. Geophys. Res.*, 84: 3532-3536.
- Westerbrook, J.H. and Jorgensen, P.J., 1968. Effects of water desorption on indentation microhardness anisotropy in minerals. *Am. Mineral.*, 53: 1899-1909.
- Yoshioka, N., 1994a. Elastic behavior of contacting surfaces under normal loads: A computer simulation using three-dimensional surface topographies. *J. Geophys. Res.*, 99: 15,549-15,560.
- Yoshioka, N., 1994b. The role of plastic deformation in normal loading and unloading cycles. *J. Geophys. Res.*, 99: 15,561 - 15,568.